Industrial Chemistry & Materials

ROYAL SOCIETY OF CHEMISTRY

PAPER

View Article Online
View Journal | View Issue

Check for updates

Cite this: *Ind. Chem. Mater.*, 2023, **1**, 247

Preparation of yolk–shell urchin-like porous Co_3O_4/NiO@C microspheres with excellent lithium storage performance†

Linhe Yu,[a] Qihao Yang,[a] Guozhen Zhu *[a] and Renchao Che *[bc]

Received 21st August 2022,
Accepted 26th October 2022

DOI: 10.1039/d2im00017b

rsc.li/icm

Yolk–shell urchin-like porous Co_3O_4/NiO@C microspheres were successfully synthesized *via* a facile solvothermal method and annealing treatment under an argon atmosphere. High reversible specific capacity, long cycling stability, and excellent rate capability were achieved for the material due to its specific yolk–shell urchin-like porous structure and coated carbon layers. The pores distributed on the yolk and shell, as well as the gap between the yolk and shell, provide numerous pathways for the penetration of electrolyte, and enhance the reversible specific capacity (the initial discharge specific capacity was as high as 1405.7 mA h g^{-1} at 0.1 C). Meanwhile, the stress and volume expansion could be greatly released and relieved through the pores, and long cycling stability was achieved (a high reversible specific capacity of 502.7 mA h g^{-1} was maintained after 1000 cycles at 5 C). The coated carbon layers greatly enhance the conductivity of the yolk–shell urchin-like porous Co_3O_4/NiO microspheres, accelerate the transmission of electrons, and improve their rate performance (a reversible specific capacity of 397.5 mA h g^{-1} was achieved when the current density was increased to 10 C).

Keywords: Yolk–shell; Urchin-like; Co_3O_4/NiO@C microspheres; Anode; Lithium storage.

1 Introduction

The goals of carbon peaking and carbon neutralization have been put forward to solve the problem of global warming in recent years.[1–3] Reducing carbon emissions is an effective way to achieve such goals.[4,5] New energy vehicles powered by lithium ion batteries have been developed rapidly in recent years, which can greatly reduce carbon dioxide emissions.[6–8] However, their wide application is restricted by short range and severe capacity degradation,[9–12]with anode materials playing a vital role in improving the range and inhibiting capacity degradation.

Transition metal oxides are promising anode materials due to their high theoretical specific capacity and high safety performance.[13–19] Nevertheless, their cycling stability and rate performance are limited by their inherent severe pulverization and poor conductivity.[20,21] Porous and core–shell structures have been designed to inhibit pulverization, thus improving cycling stability.[22–26] A hierarchical porous CoO_x/C nanocomposite was prepared using a hard template method. Benefiting from the hierarchical porous structure, a high reversible specific capacity of 381 mA h g^{-1} was retained after 500 cycles at 1.0 A g^{-1}.[27] Tubular CuO/CoO core/shell arrays have been reported, with a reversible specific capacity of 1140 mA h g^{-1} obtained after 1000 cycles at 1.0 A g^{-1} due to the hollow porous structure composed of three-dimensional hierarchical tubular core/shell arrays.[28] However, the template method has the disadvantages of involving complex processes and high costs.

In this work, we prepared yolk–shell urchin-like porous Co_3O_4/NiO@C microspheres *via* a one-step solvothermal method and subsequent annealing treatment under an argon atmosphere, which has the advantages of being simple process that can be completed at low cost compared with the common template method. In addition, the yolk–shell urchin-like porous Co_3O_4/NiO@C microspheres have the advantages of both yolk–shell and urchin-like porous structures, exhibiting a high reversible specific capacity, long cycling stability, and excellent rate performance. Benefiting from the unique yolk–shell urchin-like porous structure, the specific surface area and number of active sites involved in the electrochemical reaction were greatly increased, and high reversible specific capacity was achieved. Furthermore, owing to the cavities between the yolk and shell and the pores

[a] *Institute of Advanced Materials, Jiangxi Normal University, Nanchang 330022, P. R. China. E-mail: zhuguozhen@jxnu.edu.cn*
[b] *Laboratory of Advanced Materials, Shanghai Key Lab of Molecular Catalysis and Innovative Materials, Fudan University, Shanghai 200438, PR China. E-mail: rcche@fudan.edu.cn*
[c] *Department of Materials Science, Fudan University, Shanghai 200438, PR China*
† Electronic supplementary information (ESI) available. See DOI: https://doi.org/10.1039/d2im00017b

distributed on the surface of the yolk and shell, the stress and volume expansion during the charging/discharging process could be effectively released and relieved, respectively, to achieve long cycling stability. In addition, the coated carbon layers on the surface of microspheres greatly accelerated the transfer of electrons, promoted the ion diffusion kinetics, and improved the rate performance.

2 Results and discussion

The X-ray diffraction (XRD) patterns of yolk–shell urchin-like porous Co_3O_4/NiO (YSUCNO), yolk–shell urchin-like porous Co_3O_4/NiO@C (YSUCNO@C), Co_3O_4/NiO (CNO) microspheres are shown in Fig. 1. Similar diffraction peaks are observed for the three types of microspheres, indicating that the carbon layers coated on the surface of the YSUCNO microspheres are amorphous, and that the crystal structure was not changed by the coating of the carbon layers. The diffraction peaks located at 31.3°, 59.4°, 65.2° were ascribed to the (220), (511), (400) crystal planes of Co_3O_4 (PDF#43-1003), and the diffraction peaks at 37.2°, 43.3°, 62.9°, 75.4°, 79.4° corresponded to the (111), (200), (220), (311), (222) crystal planes of NiO (PDF#47-1049), respectively. No other diffraction peaks appeared except for those of Co_3O_4 and NiO, showing the successful synthesis of the pure YSUCNO, YSUCNO@C, CNO microspheres. However, the diffraction peak intensity of the YSUCNO@C microspheres was significantly lower than that of the YSUCNO microspheres, which was the result of the coating of the material with carbon layers.

The scanning electron microscopy (SEM) images of the YSUCNO, YSUCNO@C, and CNO microspheres are shown in Fig. 2. The yolk–shell urchin-like porous microspheres were observed (Fig. 2a and S1a†), and numerous nanopores were found to be distributed on the surface of the yolk and shell (Fig. 2b), the cavity between yolk and shell was about 500 nm wide. Compared with the YSUCNO microspheres, YSUCNO@C exhibited a larger particle size (Fig. 2c and d), which could be ascribed to the thermal treatment process. Nanorods with a diameter of 500 nm were firmly embedded on the surface of the microspheres, with the gap between nanorods being beneficial to the improvement in cycling stability. Meanwhile, the pores distributed on the surface of

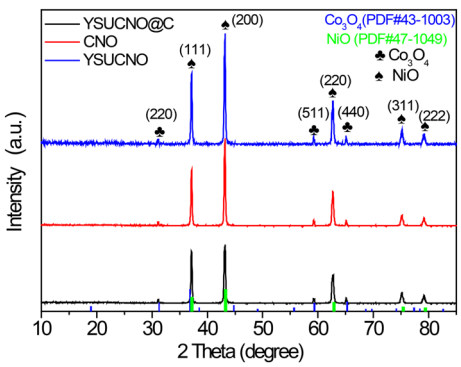

Fig. 1 XRD patterns of the YSUCNO, YSUCNO@C, and CNO microspheres.

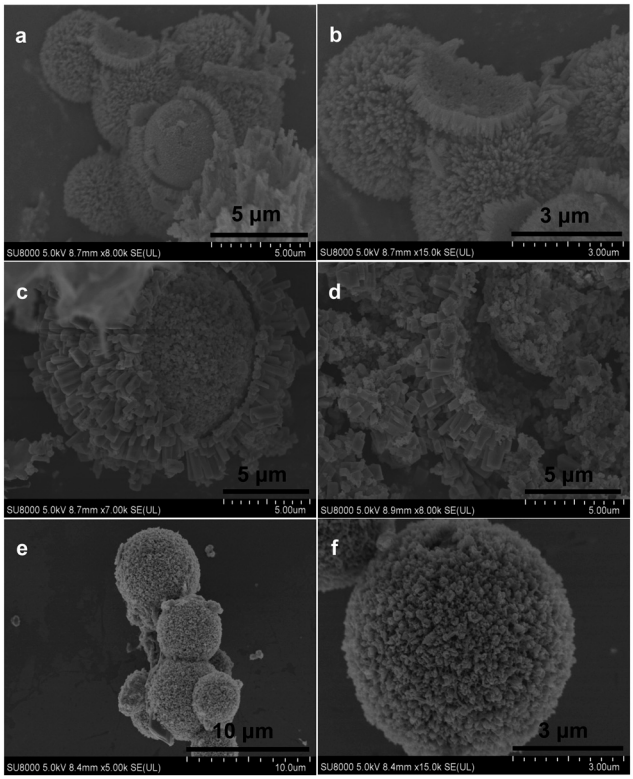

Fig. 2 SEM images of the (a and b) YSUCNO, (c and d) YSUCNO@C, and (e and f) CNO microspheres.

yolk and shell, and the cavities between the yolk and shell were conductive to releasing the stress relieving the volume expansion from the charging/discharging process, and improving the cycling stability of the microspheres.

Nitrogen adsorption/desorption curves of the YSUCNO@C, YSUCNO, and CNO microspheres are shown in Fig. S2a,† where the specific surface area of YSUCNO@C microspheres (61.2 $m^2\ g^{-1}$) can be observed to be slightly lower than that of the YSUCNO microspheres (69.8 $m^2\ g^{-1}$), and significantly higher than that of the CNO microspheres (13.6 $m^2\ g^{-1}$). The contribution from double layer capacitance is quite large, with both yolk and shell surfaces providing a large number of active sites, which are conductive to the storage of more lithium ions, thus increasing the specific capacity. The pore size distribution of the YSUCNO@C microspheres is shown in Fig. S2b,† where the average pore size of 20 nm can be observed. Porous CNO microspheres with a diameter of 2 μm to 8 μm were successfully prepared (Fig. 2e), with abundant pores distributed on the surface of the microspheres (Fig. 2f and S1b†), which were formed *via* the stacking of primary CNO nanoparticles during the spray drying process.

Fig. S3† shows the high-resolution transmission electron microscopy image of the YSUCNO@C microspheres. The obvious lattice fringes with crystal plane spacings of 0.17 nm and 0.40 nm correspond to the (220) crystal planes of the spinel cubic structure Co_3O_4 and the (311) crystal plane of NiO, respectively. The Raman spectra of the YSUCNO, YSUCNO@C, and CNO microspheres are shown in Fig. S4.†

Compared with the YSUCNO and CNO microspheres, the YSUCNO@C microspheres show significant D-band and G-band peaks of carbon, indicating that the carbon layers were successfully coated on the surface of the microspheres. The disordered D-band peak at 1330 cm^{-1} implies that the carbon atoms feature crystal defects, which are conductive to accelerating the diffusion of lithium ions, promoting the transfer of electrons, and improving the lithium storage capacity.[29–32] The thermogravimetry curve of the YSUCNO@C microspheres was measured to determine the coated carbon content (Fig. S5†), with the two weight losses corresponding to adsorbed water and coated carbon layers, and a coated carbon content of 6.06% was determined.

The cycling stability curves of the YSUCNO, YSUCNO@C, and CNO microspheres are shown in Fig. 3a. Similar to most transition metal oxides, the specific capacities of the synthesized three types of microspheres first decreased and then gradually increased during the first few cycles, illustrating that the microspheres were being activated.[33–38] The Coulomb efficiency of the first cycle of the three types of microspheres was lower than 80%, which was ascribed to the formation of a solid electrolyte interface.[39] The initial reversible specific capacities of the YSUCNO, YSUCNO@C, and CNO microspheres were found to be 1387.5 mA h g^{-1}, 1405.7 mA h g^{-1}, 1367.6 mA h g^{-1}, and the reversible specific capacities of 1013.6 mA h g^{-1}, 1246.4 mA h g^{-1}, 643.6 mA h g^{-1} were retained at 0.1 C after 200 cycles, respectively. The YSUCNO@C microspheres showed the highest capacity retention (88.7%). The cycling stability of 1000 cycles at 5 C was measured to further identify the long cycling life of the YSUCNO@C microspheres (Fig. 3b). The high reversible specific capacity of 502.7 mA h g^{-1} was maintained after 1000 cycles at 5 C due to the yolk–shell urchin-like porous structure. Abundant pores were found to be distributed on the surface of the yolk and shell, which were conductive to releasing the stress from the long-term charge/discharge processes. Meanwhile, the large cavity between yolk and shell provided enough buffer space for relieving the volume expansion of the microspheres, thus leading to long cycling stability. Most of the urchin-like structure was still retained after 1000 cycles at 5 C (Fig. S6†), exhibiting the superior cycling stability of the YSUCNO@C microspheres.

The rate performances of the YSUCNO, YSUCNO@C, and CNO microspheres are shown in Fig. 4a. The charge/discharge specific capacities gradually decreased with an increase in current density, which could be ascribed to electrode polarization. YSUCNO@C microspheres showed the highest reversible specific capacity among the three microspheres at different current densities. The average reversible specific capacities of the YSUCNO@C microspheres were 1320.2 mA h g^{-1}, 1072.3 mA h g^{-1}, 861.7 mA h g^{-1}, 656.1 mA h g^{-1}, and 397.5 mA h g^{-1} at 0.1 C, 0.5 C, 2 C, 5 C, and 10 C, respectively, and an average reversible specific capacity of as high as 1262.1 mA h g^{-1} was recovered when the current density decreased to 0.1 C. Comparatively speaking, the YSUCNO microspheres exhibited average reversible specific capacities of 1241.8 mA h g^{-1}, 931.7 mA h g^{-1}, 621.2 mA h g^{-1}, 435.4 mA h g^{-1}, and 150.7 mA h g^{-1} at 0.1 C, 0.5 C, 2 C, 5 C, and 10 C, respectively, and the average reversible specific capacity could only be recovered to 1132.1 mA h g^{-1} when the current density decreased to 0.1 C. Thus, the YSUCNO@C microspheres exhibited the best rate capability. Besides this, a rate capability comparison of the reported cobalt nickel oxide materials and $CSHCo_3O_4$@C microspheres is shown in Table S1.† The YSUCNO@C microspheres exhibit more excellent rate capability than the reported cobalt oxide materials, which can be ascribed to the special yolk–shell urchin-like porous structure and coated carbon layers. Table S2† exhibits a TMO-based cell performance comparison between the YSUCNO@C microspheres and other reported work at a high rate. The YSUCNO@C microspheres show the most superior lithium storage performance, illustrating the advantage of the special yolk–shell urchin-like structure.

Fig. 4b exhibits the cyclic voltammetry curves of the first three cycles of the YSUCNO@C microspheres. The reduction peaks located at 0.87 V and 1.19 V of the first cathode scan

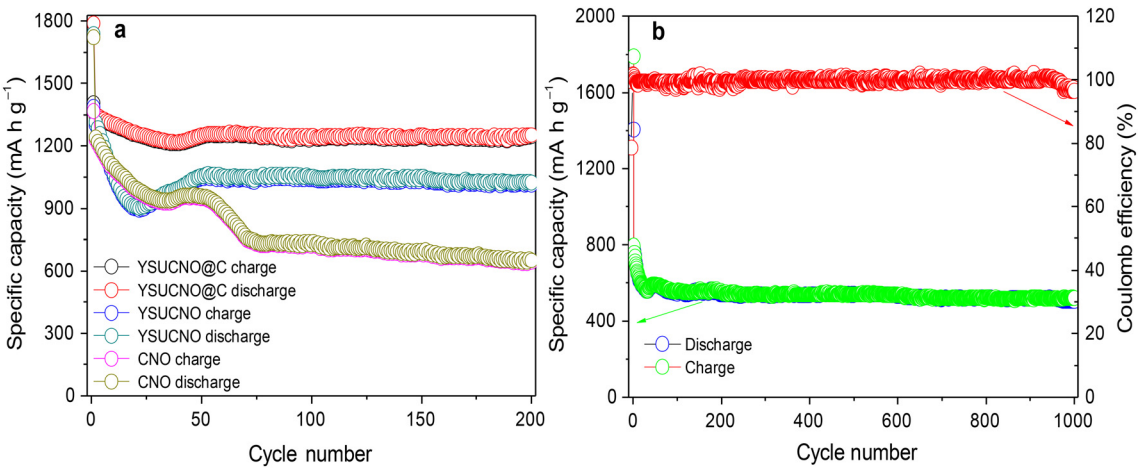

Fig. 3 Cycling stability curves of (a) the YSUCNO, YSUCNO@C, and CNO microspheres at 0.1 C for 200 cycles and (b) the YSUCNO@C microspheres at 5 C for 1000 cycles.

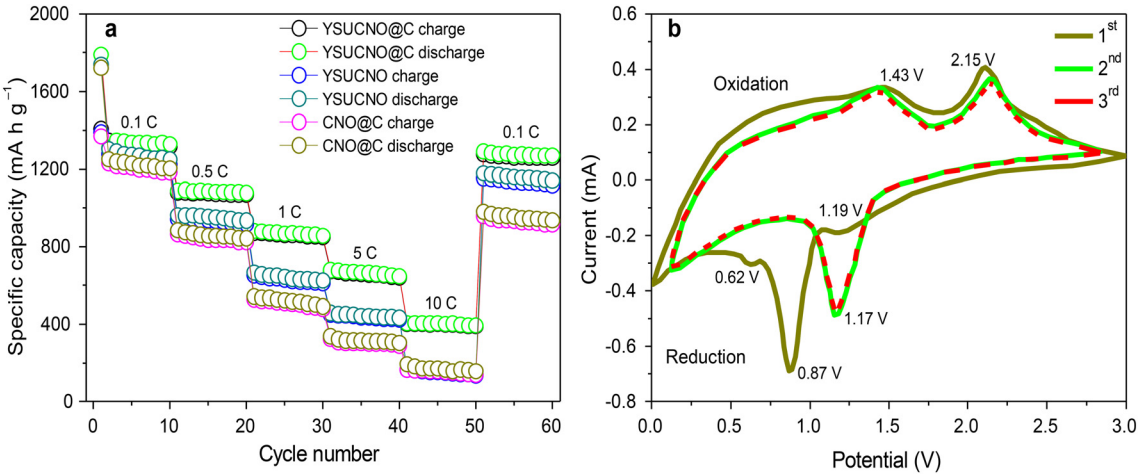

Fig. 4 (a) Rate performance of the YSUCNO, YSUCNO@C, and CNO microspheres and (b) the cyclic voltammetry curves of the first three cycles of the YSUCNO@C microspheres.

belong to the reduction of Co_3O_4/Co and NiO/Ni, respectively, and the peak at 0.62 V can be attributed to the formation of solid electrolyte interface films. From the second cycle, the reduction peak intensity gradually decreased and shifted to 1.17 V, and the reduction peaks of the last two cathode scans basically coincided, illustrating the formation of stable solid electrolyte interface films. The oxidation peaks at 1.43 V and 2.15 V of the first anode scan represented the oxidation of Co/Co_3O_4 and Ni/NiO, respectively. The three anode scans showed good coincidence, illustrating the long cycling stability of the YSUCNO@C microspheres.

Fig. 5 shows the electrochemical impedance patterns of the YSUCNO, YSUCNO@C, and CNO microspheres, which all feature a semicircle expressing the charge transfer resistance and a straight line indicating the Warburg impedance. The charge transfer resistance was found to be proportional to the size of the semicircle, and the Warburg impedance decreased with the decrease in the straight line slope. The YSUCNO@C microspheres exhibited the smallest semicircle size among the three types of microspheres, indicating that it showed the lowest charge transfer resistance and the fastest charge transfer, which was ascribed to the coated carbon layers. Meanwhile, the lowest straight line slope was observed for the YSUCNO@C microspheres, indicating that it exhibited the lowest Warburg impedance and the fastest lithium ion diffusion. The σ (Warburg coefficient) values of the YSUCNO, YSUCNO@C, and CNO microspheres calculated using the Warburg coefficient are shown in Fig. S7.† According to the equation $D = R^2T^2/2A^2n^4F^4C^2\sigma^2$, the lithium ion diffusion coefficient increases with a decrease in the σ value, and the YSUCNO@C microspheres exhibit the minimum σ value among the three types of microspheres, showing the maximum Li-ion diffusion coefficient and the strongest Li-ion diffusion capability of the YSUCNO@C microspheres. D represents ionic diffusion coefficient, R represents gas constant (8.314 kJ^{-1} mol^{-1}), T represents Kelvin temperature, A represents electrode area, n represents number of electrons transferred in the reaction process, F represents Faraday constant (500 C mol^{-1}), C represents lithium ion phase concentration, and σ represents the Warburg coefficient. The σ values of the YSUCNO, YSUCNO@C, and CNO microspheres increased significantly after 100 cycles (Fig. S8†). By comparison, the σ value of the CNO microspheres increased significantly, showing that the YSUCNO@C microspheres exhibited the lowest volume change among the three materials.

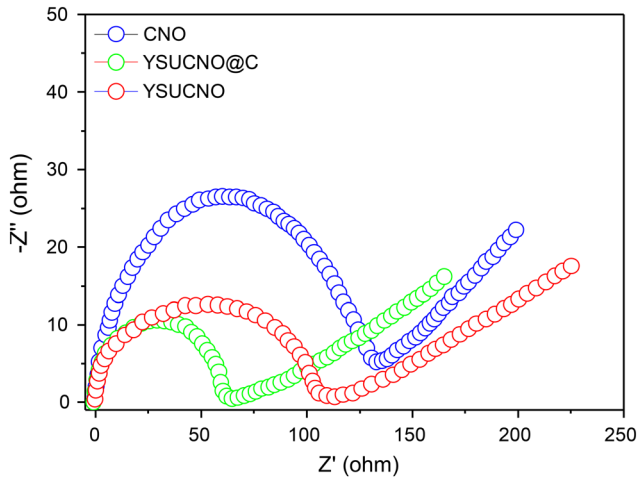

Fig. 5 Impedance patterns of the YSUCNO, YSUCNO@C, and CNO microspheres.

The YSUCNO@C microspheres exhibited the longest cycling stability and the best rate performance among the three types of microspheres, which could be ascribed to the following reasons. i) Benefiting from the unique yolk–shell urchin-like porous structure, high initial reversible specific capacity was achieved. Benefiting from the abundant pores distributed on the yolk and shell, as well as the cavities between the yolk and shell, a high large surface specific area could be achieved, and full contact between the active

substance and electrolyte was ensured, thus leading to high reversible specific capacity being achieved. ii) The yolk–shell urchin-like porous structure was conductive to improving the cycling stability. Numerous pores were found to be distributed on the surface of the yolk and shell, and the cavities between the yolk and shell greatly released the stress, effectively relieving the volume expansion from the long-term charging/discharging processes, thus ensuring the stability of the microsphere structure and the improvement in the cycling stability. iii) The coated carbon layers on the surface of YSUCNO microspheres contributed to the improvement in the rate performance. The conductivity was effectively improved *via* the coating of the carbon layers, and the transfer speed of the electrons was significantly promoted, with the rate performance thus being enormously improved.

3 Conclusions

In short, yolk–shell urchin-like Co_3O_4/NiO@C microspheres were prepared *via* a one-step solvothermal method and annealing treatment. The pores distributed on the surface of the yolk and shell, as well as the cavities between the yolk and shell, not only provided pathways for the penetration of electrolyte, but also relieved the volume expansion from the charge/discharge processes, thus leading to a high initial reversible specific capacity and long cycling life. A high initial reversible specific capacity of 1405.7 mA h g^{-1} was achieved at 0.1 C, and a reversible specific capacity as high as 502.7 mA h g^{-1} was retained after 1000 cycles at 5 C. What is more, the rate performance was greatly improved due to the coated carbon layers. The reversible specific capacity of 397.5 mA h g^{-1} was still retained even when the current density was increased to 10 C.

4 Experimental section

4.1 Materials

Cobalt chloride, cobalt nitrate, sodium dodecyl benzene sulfonate, 2-methylimidazole, nickel chloride, *N*,*N*-dimethyl bromide methyl formamide, 1,3,5-benzoic acid, and absolute ethanol were all purchased from Sigma. Deionized water, prepared in the laboratory, was used throughout the experiments.

4.2 Synthesis of the yolk–shell urchin-like porous Co_3O_4/NiO@C microspheres

The synthesis process of the yolk–shell urchin-like porous Co_3O_4/NiO@C microspheres is shown in Fig. 6a. Cobalt chloride, nickel chloride, 2-methylimidazole, 1,3,5-benzoic acid, and sodium dodecyl benzene sulfonate were all transferred into the *N*,*N*-dimethyl bromide methyl formamide, with the resulting mixture continuously stirred for 2 h to obtain a homogeneous blue solution. Subsequently, the blue solution was poured into a sealed 100 mL stainless steel autoclave, which was heated at 180 °C for 24 h. Then, a yolk–shell urchin-like Co_3O_4/NiO microsphere powder was obtained *via* alternating centrifugation treatment using absolute ethanol and deionized water three times and vacuum drying at 70 °C

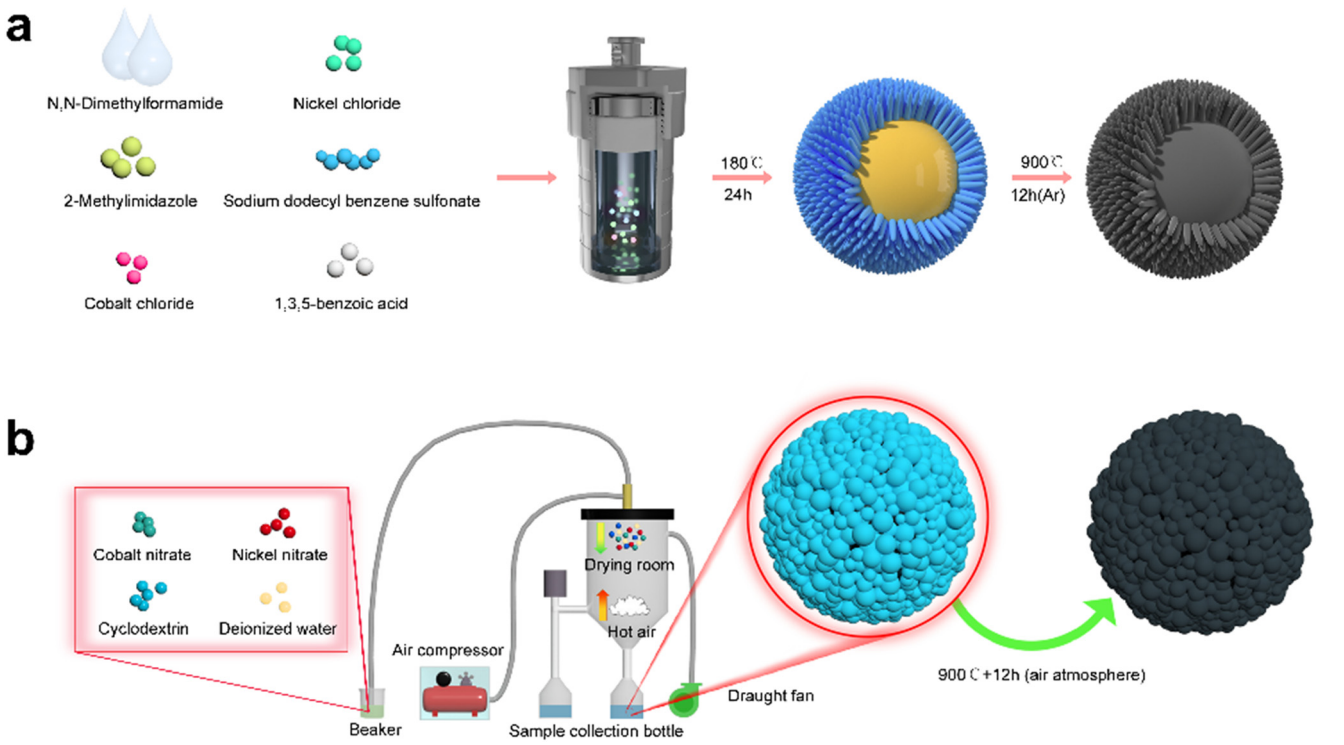

Fig. 6 Synthesis process of the (a) yolk–shell urchin-like porous Co_3O_4/NiO@C and (b) porous Co_3O_4/NiO microspheres.

for 12 h. Finally, the Co_3O_4/NiO microsphere powder was mixed with cyclodextrin, and continuously ground for 60 min to obtain a mixed powder, which was then annealed at 900 °C for 12 h under an argon atmosphere to prepare the yolk–shell urchin-like porous Co_3O_4/NiO@C microspheres (denoted as YSUCNO@C microspheres).

4.3 Synthesis of the porous Co_3O_4/NiO microspheres

The synthesis process of the porous Co_3O_4/NiO microspheres is shown in Fig. 6b. Firstly, cobalt nitrate, nickel nitrate, and cyclodextrin were dissolved in deionized water to obtain a mixed solution. Then, the mixed solution was sprayed into a Co_3O_4/NiO microsphere precursor using a spray dryer. Finally, the microsphere precursor was annealed at 900 °C for 12 h in air to prepare the porous Co_3O_4/NiO microspheres (denoted as CNO microspheres).

4.4 Materials characterization

The phase purity of the prepared samples was analyzed by XRD (Bruker D8 Advance). The morphology of the prepared samples was observed by field-emission scanning electron microscopy (Hitachi, S-4800) and transmission electron microscopy (JEOL, JEM-2100F). The porosity of the structure was identified using a specific surface analyzer (ASAP2020). The element valence was determined by X-ray photoelectron spectroscopy (Axis Ultra DLD).

4.5 Measurement of the electrochemical performance

Active substance, acetylene black, polyvinylidene fluoride, and *N*-methylpyrrolidone were mixed together and mechanical stirred for 100 min until the slurry showed good fluidity. Then, the slurry was scraped on the surface of copper foil, before being vacuum dried at 75 °C for 12 h to obtain the film. The film was punched into discs with a diameter of 12 nm, and vacuum dried at 75 °C for 12 h. Finally, the discs, microporous polypropylene film, $LiFP_6$, and metallic lithium sheet were assembled into button batteries in a glovebox filled with argon gas. The cyclability and rate performance of the button batteries were tested using a Land battery system (CT2001A). The cyclic voltammetry curves of the button batteries were analyzed on an electrochemical workstation (CHI604D).

Conflicts of interest

The authors declare no conflict of interest.

Acknowledgements

This work was supported by the National Natural Science Foundation of China (51725101, 11727807, 51672050, 61790581), the Ministry of Science and Technology of China (973 Project No. 2018YFA0209102), and the science and technology research project of Jiangxi Provincial Department of Education (GJJ200338).

References

1 X. Lyu, K. Yang and J. Fang, Utilization of Resources in Abandoned Coal Mines for Carbon Neutrality, *Sci. Total Environ.*, 2022, **822**, 153646.
2 B. Chen, H. Zhang, W. Li, H. Du, H. Huang, Y. Wu and S. Liu, Research on Provincial Carbon Quota Allocation Under the Background of Carbon Neutralization, *Energy Rep.*, 2022, **8**, 903–915.
3 Y. Tian, D. Xie, T. Li, J. Li, Y. Zhang, H. Jing, D. Zhong and G. Wang, Achieving Chinese Carbon Neutrality Based on Water-Temperature-Radiation-Land Coupling Use, *Front. Environ. Sci.*, 2021, **9**, 740665.
4 Z. Sun, L. J. Sun, S. W. Koh, J. Ge, J. Fei, M. Yao, W. Hong, S. Liu, Y. Yamauchi and H. Li, Photovoltaic-powered supercapacitors for driving overall water splitting: A dual-modulated 3D architecture, *Carbon Energy*, 2022, 1–12, DOI: 10.1002/cey2.213.
5 Z. Sun, K. Li, S. W. Koh and L. Jiao, A Green and Simple Method for Energy Storage and Conversion Application, *J. Mater. Sci.*, 202, **56**, 3354–3363.
6 Y. Li, J. Song and J. Yang, A Review on Structure Model and Energy System Design of Lithium-Ion Battery in Renewable Energy Vehicle, *Renewable Sustainable Energy Rev.*, 2014, **37**, 627–633.
7 X. Zeng, M. Li, D. Abd El-Hady, W. Alshitari, A. S. Al-Bogami, J. Lu and K. Amine, Commercialization of Lithium Battery Technologies for Electric Vehicles, *Adv. Energy Mater.*, 2019, **9**, 1900161.
8 Y. Li, J. Yang and J. Song, Design Principles and Energy System Scale Analysis Technologies of New Lithium-Ion and Aluminum-Ion Batteries for Sustainable Energy Electric Vehicles, *Renewable Sustainable Energy Rev.*, 2017, **71**, 645–651.
9 Y. Xing, A. T. Jenn, Y. Wang, C. Li, S. Sun, X. Ding and S. Deng, Optimal Range of Plug-in Electric Vehicles in Beijing and Shanghai, *Mitigation and Adaptation Strategies for Global Change*, 2020, **25**, 441–458.
10 F. Morlock, B. Rolle, M. Bauer and O. Sawodny, Time Optimal Routing of Electric Vehicle Under Consideration of Available Charging Infrastructure and a Detailed Consumption Model, *IEEE Trans. Intell. Transp. Syst.*, 2020, **21**, 5123–5135.
11 P. R. Shearing and L. R. Johnson, Toward Practical Demonstration of High-Energy-Density Batteries, *Joule*, 2020, **4**, 1359–1361.
12 D. L. Greene, E. Kontou, B. Borlaug, A. Brooker and M. Muratori, Public Charging Infrastructure for Plug-in Electric Vehicles: What is it worth?, *Transp. Res. D*, 2020, **78**, 102182.
13 R. J. Clement, Z. Lun and G. Ceder, Cation-Disordered Rocksalt Transition Oxides and Oxyfluorides for High Energy Lithium-Ion Cathodes, *Energy Environ. Sci.*, 2020, **13**, 345–373.
14 X. Tan, Y. Wu, X. Lin, A. Zeb, X. Xu, Y. Luo and J. Luo, Application of MOF-Derived Transition Metal Oxides and Composites as Anode for Lithium-Ion Batteries, *Inorg. Chem. Front.*, 2021, **7**, 4939–4955.

15 T. Li, Y. Bai, Y. Wang, H. Xu and H. Jin, Advances in Transition-Metal (Zn, Mn, Cu)-Based MOFs and Their Derivatives for Anode of Lithium-Ion Batteries, *Coord. Chem. Rev.*, 2020, **410**, 213221.

16 J. Yu, S. Chen, W. Hao and S. Zhang, Fibrous-Root-Inspired Design and Lithium Storage Applications of a Co-Zn Binary Synergistic Nanoarray System, *ACS Nano*, 2016, **10**, 2500–2508.

17 Y. Wei, F. Yan, X. Tang, Y. Luo, M. Zhang, W. Wei and L. Chen, Solvent-Controlled Synthesis of NiO-CoO/Carbon Fiber Nanobrushes with Different Densities and Their Excellent Properties for Lithium Ion Storage, *ACS Appl. Mater. Interfaces*, 2015, **7**, 21703–21711.

18 X. Xu, B. Dong, S. Ding, C. Xiao and D. Yu, Hierarchical $NiCoO_2$ Nanosheets Supported on Amorphous Carbon Nanotubes for High-Capacity Lithium-Ion Batteries with a Long Cycle Life, *J. Mater. Chem. A*, 2014, **2**, 13069–13074.

19 M. Zhang, D. Li, L. Yang, H. Shi and Y. Liu, Dendritic Micro-Nano $NiCo_2O_4$ Anode Material Generated from Chemical Dealloying for High-Performance Lithium-Ion Batteries, *Ionics*, 2020, **26**, 5385–5392.

20 H. Ye, G. Zheng, X. Yang, D. Zhang, Y. Zhang, S. Yan, L. You, S. Hou and Z. Huang, Application of Different Carbon-Based Transition Metal Oxide Composite Materials in Lithium-Ion Batteries, *J. Electroanal. Chem.*, 2021, **898**, 115652.

21 C. Zhang, J. Chen, Y. Zeng, X. Rui, J. Zhu, W. Zhang, C. Xu, T. M. Lim, H. H. Hng and Q. Yan, A Facile Approach Toward Transition Metal Oxide Hierarchical Structures and Their Lithium Storage Properties, *Nanoscale*, 2012, **4**, 3718–3724.

22 D. Wu, J. Song, Y. Ji, Q. Tian, Z. Sui, J. Z. Chen and L. Yang, Engineering Hollow Cobalt Oxide Nanospheres with Porous Carbon Coating for Stable Lithium Storage, *J. Electroanal. Chem.*, 2021, **895**, 115531.

23 X. Zuo, Y. Song and M. Zhen, Carbon-Coated $NiCo_2S_4$ Multi-Shelled Hollow Microspheres with Porous Structures for High Rate Lithium Ion Battery Applications, *Appl. Surf. Sci.*, 2019, **500**, 144000.

24 H. Liu, X. Wang, J. Wang, H. Xu, W. Yu, X. Dong, H. Zhang and L. Wang, Hierarchical Porous CoNi/CoO/NiO Composites Derived from Dealloyed Quasicrystals as Advanced Anodes for Lithium-Ion Batteries, *Scr. Mater.*, 2017, **139**, 30–33.

25 Y. Wang, Y. Wang, L. Lu, B. Zhang, C. Wang, B. He, R. Wei, D. Xu, Q. Hao and B. Liu, Hierarchically Hollow and Porous $NiO/NiCo_2O_4$ Nanoprisms Encapsulated in Graphene Oxide for Lithium Storage, *Langmuir*, 2020, **36**, 9668–9674.

26 H. Du, K. Huang, W. Dong and B. Geng, A General Gelatin-Assisted Strategy to Hierarchical Porous Transition Metal Oxides with Excellent Lithium-Ion Storage, *Electrochim. Acta*, 2018, **279**, 66–73.

27 X. Fan, K. Ni, H. Yang, L. Lu and S. Li, Hierarchical Porous CoO_x/Carbon Nanocomposite for Enhanced Lithium Storage, *J. Electroanal. Chem.*, 2019, **847**, 113202.

28 J. Wang, Q. Zhang, X. Li, B. Zhang, L. Mai and K. Zhang, Smart Construction of Three-Dimensional Hierarchical Tubular Transition Metal Oxide Core/Shell Heterostructures with High-Capacity and Long-Cycle-Life Lithium Storage, *Nano Energy*, 2015, **12**, 437–446.

29 J. Ou, S. Wu, L. Yang and H. Wang, Facile Preparation of NiO@Graphene Nanocomposite with Superior Performance as Anode for Li-Ion Batteries, *Acta Metall. Sin.*, 2021, **35**, 212–222.

30 Y. Wang, M. Kong, Z. Liu, C. Lin and Y. Zeng, Morella-Rubra-Like Metal-Organic-Framework-Derived Multilayered Co_3O_4/NiO/C Hybrids as High-Performance Anodes for Lithium Storage, *J. Mater. Chem. A*, 2017, **5**, 24269–24274.

31 Y. Wang and L. Zhang, Simple Synthesis of CoO-NiO-C Anode Materials for Lithium-Ion Batteries and Investigation on its Electrochemical Performance, *J. Power Sources*, 2012, **209**, 20–29.

32 Y. Xie, J. Cao, X. Wang, W. Li, L. Deng, S. Ma, H. Zhang, C. Guan and W. Huang, MOF-Derived Bifunctional $Co_{0.85}Se$ Nanoparticles Embedded in N-Doped Carbon Nanosheet Arrays as Effiffifficient Sulfur Hosts for Lithium-Sulfur Batteries, *Nano Lett.*, 2021, **21**, 8579–8586.

33 D. Wang, H. He, L. Han, R. Lin, J. Wang, Z. Wu, H. Liu and H. L. Xin, Three-Dimensional Hollow-Structured Binary Oxide Particles as an Advanced Anode Material for High-Rate and Long Cycle Life Lithium-Ion Batteries, *Nano Energy*, 2016, **20**, 212–220.

34 K. Cao, T. Jin, L. Yang and L. Jiao, Recent Progress in Conversion Reaction Metal Oxide Anodes for Li-Ion Batteries, *Mater. Chem. Front.*, 2017, **1**, 2213–2242.

35 X. Xu, H. Tan, K. Xi, S. Ding, D. Yu, S. Cheng, G. Yang, X. Peng, A. Fakeeh and R. Vasant, Bamboo-Like Amorphous Carbon Nanotubes Clad in Ultrathin Nickel Oxide Nanosheets for Lithium-Ion Battery Electrodes with Long Cycle Life, *Carbon*, 2015, **84**, 491–499.

36 W. Liu, F. Yuanyuan, Y. Li, S. Chen, Y. Song and L. Wang, Three-Dimensional Carbon Foam Surrounding by Carbon Nanotubes and Co-Co_3O_4 Nanoparticles for Stable Lithium-Ion Batteries, *Composites, Part B*, 2019, **163**, 464–470.

37 Q. Deng, M. Wang, Z. Peng, Z. Liu, H. Fan and Y. Zhang, Ultrafast Li^+ Diffusion Kinetics Enhanced by Cross-Stacked Nanosheets Loaded with Co_3O_4@NiO Nanoparticles: Constructing Superstructure to Enhance Li-Ion Half/Full Batteries, *J. Colloid Interface Sci.*, 2021, **585**, 51–60.

38 H. Liu, X. Wang, H. Xu, W. Yu, X. Dong, Y. Yang, H. Zhang and J. Wang, Nanostructured CoO/NiO/CoNi Anodes with Tunable Morphology for High Performance Lithium-Ion Batteries, *Dalton Trans.*, 2017, **46**, 11031–11036.

39 J. Cao, Y. Xie, Y. Yang, X. Wang, W. Li, Q. Zhang, S. Ma, S. Cheng and B. Lu, Achieving Uniform Li Plating/Stripping at Ultrahigh Currents and Capacities by Optimizing 3D Nucleation Sites and Li_2Se-Enriched SEI, *Adv. Sci.*, 2022, **9**, 2104689.